Solar Energy Materials and Solar Cells 201 (2019) 110051

Contents lists available at ScienceDirect

Solar Energy Materials and Solar Cells

journal homepage: www.elsevier.com/locate/solmat

Thermal emissivity of silicon heterojunction solar cells

D. Alonso-Álvarez[a,*], A. Augusto[b], P. Pearce[a], L. Ferre Llin[c,2], A. Mellor[a,1], S. Bowden[b], D.J. Paul[c], N. Ekins-Daukes[a,d]

[a] Department of Physics, Imperial College London, London, SW7 2AZ, UK
[b] Arizona State University, Electrical Engineering, P.O. Box 875706, Tempe, AZ, 85287-5706, USA
[c] School of Engineering, University of Glasgow, Glasgow, G12 8LT, UK
[d] School of Photovoltaic & Renewable Energy Engineering, UNSW Sydney, Kensington, NSW, 2052, Australia

ARTICLE INFO

Keywords:
Solar cells
Silicon
Emissivity
Heterojunction
Modelling

ABSTRACT

The aim of this work is to evaluate whether silicon heterojunction solar cells, lacking highly emissive, heavily doped silicon layers, could be better candidates for hybrid photovoltaic thermal collectors than standard aluminium-diffused back contact solar cells. To this end, the near and mid infrared emissivity of full silicon heterojunction solar cells, as well as of its constituent materials – crystalline silicon wafer, indium tin oxide, n-, i- and p-type amorphous silicon – have been assessed by means of ellipsometry and FTIR. The experimental results show that the thermal emissivity of these cells is actually as high as in the more traditional structures, ~80% at 8 μm. Detailed optical modelling combining raytracing and transfer matrix formalism shows that the emissivity in these cells originates in the transparent conductive oxide layers themselves, where the doping is not high enough to result in a reflection that exceeds the increased free carrier absorption. Further modelling suggests that it is possible to obtain lower emissivity solar cells, but that a careful optimization of the transparent conductive layer needs to be done to avoid hindering the photovoltaic performance.

1. Introduction

Thermal emissivity of solar cells is gaining interest both due to its effect on the normal cell operating temperature, and therefore efficiency in the field [1], and due to its effect on the thermal performance of hybrid photovoltaic-thermal (PV-T) collectors [2,3]. We have shown in recent experiments that radiative emissivity of aluminium-diffused back contact solar cells is extremely high, and have deduced from modelling that this originates from the highly doped emitter and back surface field layers [4]. Silicon heterojunctions (SHJ) solar cells offer an excellent opportunity to boost the performance of hybrid PV-T collectors for two reasons. First, their low thermal coefficient of power will help to keep high efficiency at elevated temperatures. The impact of this property in PV-T systems has been analysed in detailed by Mellor et al. [2]. Second, SHJ cells are expected to have lower mid-infrared (MIR) emissivity than the traditional silicon solar cell design as they lack highly doped silicon layers and instead have a front indium tin oxide layer, which is a material often used as a low emissivity coating.

In this work we assess the latter hypothesis by measuring the MIR emissivity of a state-of-the-art SHJ solar cell, together with their individual components. Integrated raytracing and transfer-matrix method simulations are used to get further insight into the role and impact of each of the layers that make the structure.

2. Materials and methods

2.1. Samples fabrication

Three sets of samples were fabricated in order to evaluate in detail the mid infrared properties of SHJ solar cells: (1) standard SHJ solar cell (sample 1), (2) standard SHJ without front ITO and contacts (sample 2), and (3) test samples consisting of a silicon substrate with silver sputtered on the back and only one of the layers needed to make the SHJ cell deposited on top (sample 3a to 3f). Sample 3a is just the substrate with the silver back layer. Fig. 1 shows a schema of these samples and Table 1 the nominal thickness of all the layers. Samples 1 and 2 were manufactured on commercial grade < 100 > n-type Czochralski (CZ) wafers with 3–4 Ω cm resistivity (doping level 1.15×10^{15} to 1.5×10^{15} cm^{-3}). The alkaline texturing and saw damage removal were followed by wet chemical cleaning and conditioning. After the chemical process the wafers were 170 μm thick.

* Corresponding author.
E-mail address: d.alonso-alvarez@imperial.ac.uk (D. Alonso-Álvarez).
[1] Now at: Naked Energy Ltd. Basepoint Business Centre, Metcalf Way, Crawley, RH11 7XX, United Kingdom.
[2] Now at: ASML Netherlands, De Run 6501, 5504 DR, Veldhoven, the Netherlands.

https://doi.org/10.1016/j.solmat.2019.110051
Received 3 May 2019; Accepted 7 July 2019
Available online 11 July 2019
0927-0248/

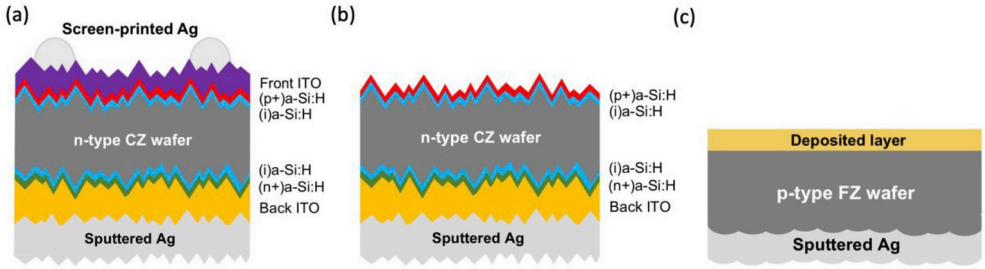

Fig. 1. Structure of the samples of this study. (a) Full SHJ cell, (b) SHJ cell without front ITO and contacts and (c) test samples.

Table 1
Nominal thickness of the layers of the different materials that make the samples.

Layer	Sample 1	Sample 2	Samples 3					
			a	b	c	d	e	f
wafer	170 µm	170 µm	685 µm	–	–	–	–	–
Front ITO	80 nm	–	–	80 nm	–	–	–	–
p-a-Si	6–7 nm	6–7 nm	–	–	20 nm	–	–	–
i-a-Si	6–7 nm	6–7 nm	–	–	–	20 nm	–	–
n-a-Si	6–7 nm	6–7 nm	–	–	–	–	20 nm	–
Back ITO	240 nm	240 nm	–	–	–	–	–	220 nm
Ag	240 nm							

The heterojunction was formed using plasma-enhanced chemical vapor deposition (PECVD) to grow intrinsic (i), p+ and n + doped hydrogenated amorphous (a-Si:H) layers (6–7 nm), forming a (p+)i/CZ/i (n+) stack. Indium tin oxide (ITO) was sputtered on both sides of the sample 1, Fig. 1 (a), and only on the back side of sample 2, Fig. 1 (b). The front ITO is 80 nm thick and it was optimized to provide good carrier collection (sheet resistance < 70 Ω/sq) and good anti-reflective properties. The back ITO is 240 nm thick and was developed to minimize the absorption in the near-infrared [5]. Silver was sputtered on the back of the samples, working as a rear reflector. For sample 1, the front contacts were screen-printed with silver paste. At the end the samples were annealed at 200 °C for 45 min. The test samples 3a to 3f were manufactured on < 100 > p-type one-side polished Float Zone (FZ) wafers with 1–3 Ω cm resistivity (doping level 1.15×10^{15} to 1.5×10^{15} cm^{-3}). In all test samples a 240 nm-thick silver layer was sputtered on the back of the wafer (unpolished side) to prevent transmission through the wafer, Fig. 1 (c). Individual layers, see Table 1, were deposited on each sample at the front of the wafer (polished side). The amorphous silicon layers were deposited by PECVD and the ITO layers by sputtering. Like samples 1 and 2, these samples were annealed at 200 °C for 45 min. It should be noted that the a-Si material was optimized to make very thin layers and that a large uncertainty in the thickness is to be expected for the layers in the test samples.

2.2. Optical characterization

The near (NIR) and mid-infrared (MIR) absorptivity (=emissivity) of the samples were measured using a Bruker Vertex 70 FTIR system equipped with a gold-coated integrating sphere and a liquid nitrogen-cooled HgCdTe detector by Infrared Associates Inc. Ellipsometry analysis was performed using two J. A. Woollam Co. Systems, a V-VASE for the UV-VIS-NIR range (300 nm–1700 nm) and an IR-VASE Mark-II for the MIR (1.7 µm–20 µm). Ellipsometric measurements were taken at three angles (45°, 60° and 75°). The data from the two systems was combined and fitted to the modelled dielectric function over the whole spectral range (300 nm–20 µm wavelength) using the WVASE software from J.A. Woollam Co.. Despite the texture at the back of the samples, in some cases there was some depolarization of the measured ellipsometry signal for the longest wavelengths, making the ellipsometry data unreliable in that range. These data points were excluded from the fitting process.

3. Modelling

The absorptivity, and therefore emissivity, of the solar cells was modelled over the wavelength range 350 nm–16 µm using the three-dimensional OPTOS formalism [6] with some additions to account for absorption in the surface textures themselves, in addition to absorption in the bulk Si of the cells. An integrated transfer matrix method (TMM) and ray-tracing approach similar to that employed in Ref. [4] was used to solve the reflection, absorption and transmission of the front and back films, grouped together in stacks (Fig. 2); however, rather than using a two-dimensional ray-tracing approach and adjusting the results for 3D using an escape factor, a full 3D ray-tracer was used, shown schematically in Fig. 2c. At each surface interaction, the ray can be reflected, transmitted, or absorbed; the probabilities are calculated using TMM at the relevant incidence angle (relative to the textured surface) and wavelength. These calculations are performed scanning across many incidence angles at each wavelength, varying both the polar and azimuthal angle of incidence; the results of the ray-tracing simulations are used to build up matrices according to the formalism from Ref. [6], describing how light incident on the front and back surfaces of the cell is redistributed into other directions. In addition, similar to the modifications made to the OPTOS formalism in Ref. [7], the matrix framework was adapted to include how light incident from each angle is absorbed in the front and back surfaces. Finally, absorption in the bulk according to the Beer-Lambert law is accounted for using a propagation matrix, allowing the full behaviour of light inside the stack can be described [6].

4. Results

4.1. Ellipsometry

Fig. 3 shows the n and k data resulted from a fitting of the ellipsometric parameters ψ and Δ. For the ITO films, the data is fitted with a Tauc-Lorentz-Drude model as in Ref. [3]. For the silicon and amorphous silicon, a general oscillator model is used including four separate oscillators [8]. Details of this fitting are shown in Appendix A. Fig. 3a and b shows the data for amorphous silicon, including a reference from Palik [9], and for the silicon substrate. Another set of data constructed from Green [11] for the short wavelength range (< 1100 nm) and Fu and Zhang [10] for the long wavelength range assuming a doping of around 10^{16} cm^{-3} is also included for comparison. The intrinsic and n-type a-Si have nearly identical optical

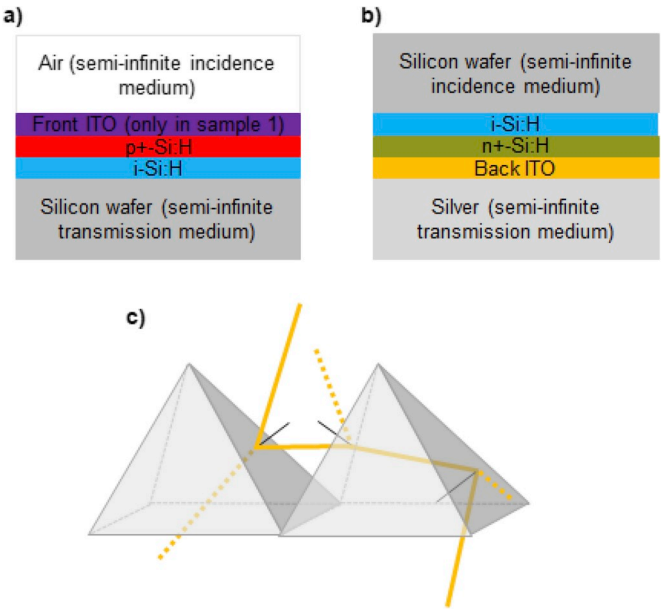

Fig. 2. Division of the SHJ solar cell structure used in the modelling, grouping a) the front layers (as seen for light incident from outside the cell) and b) the back layers (as seen for light incident from inside the cell) into stacks, for which the reflection, absorption and transmission probabilities are calculated using a TMM approach. The silver front contacts in sample 1 were not considered in the simulation. c) Schematic of three-dimensional ray-tracing for a ray incident from above on an upright pyramid texture. The dashed lines show other possible paths of the ray at each interaction with the surface.

properties and are very similar to the data measured by Palik. The estimated thicknesses, also indicated in the plot, are in reasonable agreement with the expected value or around 20 nm. However, the p-type a-Si layer is markedly different from the other two, both in the estimated thickness and the optical properties, also in disagreement with Palik. This disagreement of the p-type a-Si is attributed to the large uncertainty in the growth rate and film homogeneity. Finally, in none of the a-Si layers there is evidence of a band edge absorption in *k*, probably related to the presence of a strong Urbach tail associated to sub-gap states. This is also consequence of the ellipsometry technique, which cannot provide reliable *k* results when measuring weakly absorbing layers in combination with a very small thickness.

Fig. 3c and d shows the same information but for the two ITO films. The front-ITO film has higher doping than the back-ITO film due to the oxygen vacancies, and therefore a blue-shifted absorption edge and higher free carrier absorption at longer wavelengths. These results agree with our own results for ITO films grown at ICL [3].

4.2. MIR emissivity

All the samples were opaque due to the silver layer sputtered on the back the emissivity so ε can be estimated simply as $\varepsilon = A = 1 - R$, with A the absorptivity and R the hemispherical reflectivity. Fig. 4a shows the emissivity of the test samples with the individual films on top. All the a-Si films exhibit the same emissivity, being this around 5%–10% higher than the silicon substrate. The lack of the dependence on the type of doping suggest that the increased emissivity is not related with absorption in the a-Si films but with reduced front surface reflection. Both ITO films show increased emissivity at short wavelengths compared to the silicon substrate due to a reduced front surface reflection as a consequence of the lower refractive index. However, that trend is reversed at longer wavelengths where the effect of the free carrier absorption – increasing the imaginary part of the refractive index to levels comparable to that of the real part – becomes relevant and increases the reflection, lowering the emissivity. The free carrier reflection is dominant for the front ITO film whereas it is negligible for the back ITO.

The emissivity of SHJ cells is shown in Fig. 4b. Both cells have the same structure except for the front ITO which is absent for sample 2, as described in Fig. 1 and Table 1. The samples have random pyramidal textures on both sides. The first consequence of the texture is that, even though the substrate is thinner than in the test samples, front surface reflection is reduced, and light trapping is much more effective so that the emissivity (=absorptivity) is much higher. The cell without front ITO has an emissivity of around 45% at 2 μm that increases to a constant value of 80% from 5 μm. As with the flat samples, adding the ITO has two consequences: the emissivity increases at short wavelengths due to reduced reflection and higher absorption and it decreases at longer wavelengths due to the reflection associated with free carriers. The first one will increase the absorption of sub-bandgap solar photons, which do not contribute to the photocurrent but will heat up the solar cell. The second decreases the radiative thermal emission, both of which are desirable for PV-T systems.

5. Discussion

The results presented in Section 4.2 demonstrate that the initial hypothesis that SHJ solar cells should be better for hybrid PV-thermal applications because of the expected lower emissivity in the MIR than aluminum-diffused back contact cells should be revised: despite the absence of heavily doped layers (emitter and back surface field) and the

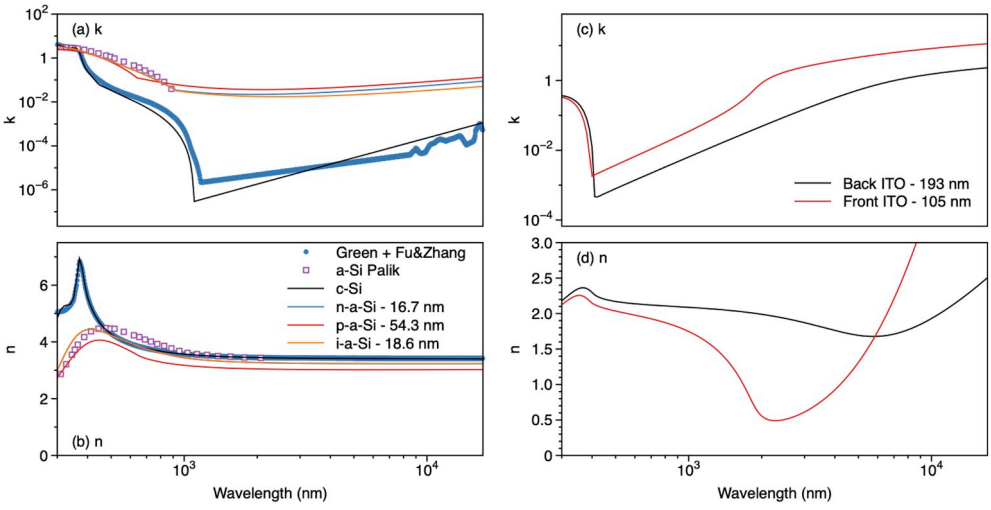

Fig. 3. (a) and (b) Calculated n, k data for the a-Si films. (c) and (d) Calculated n, k data for the ITO films.

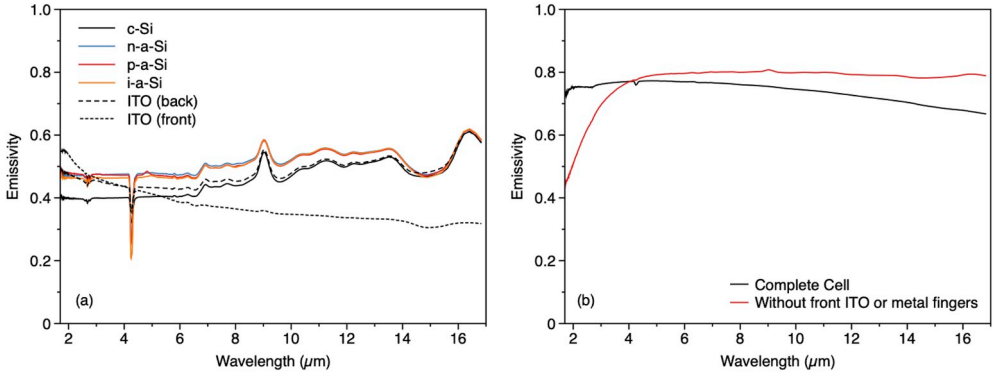

Fig. 4. (a) Emissivity of the individual films on the test samples. (b) Emissivity of full SHJ solar cells with front ITO (sample 1) and without front ITO (sample 2).

built-in ITO layers, the emissivity of the SHJ solar cells is, actually, comparable to that of a standard silicon cell [4]. Considering that the amorphous silicon layers have a very small effect in the emissivity and that in the real device they are much thinner than in the flat test samples (~6 nm), this suggests two other possible explanations: (1) the n-type doping of the wafer, while low, is high enough to result in very high emissivity when combined with texturing, which could be in agreement with reported studies [12]; or (2) that the specific combination of thicknesses and optical properties of the ITO layers promote the absorption of MIR. As described in Alonso-Álvarez et al. it is not enough to have highly doped transparent conductive oxides layers in order to have low emissivity, but also these need to have a specific thickness, especially if embedded in between other layers [3].

In order to clarify this issue, the numerical modelling framework presented in Section 3 was used in combination with the experimental n and k data of the materials to elucidate the measured emissivity and identify the origin of the high emissivity in the MIR.

5.1. SHJ solar cells

Fig. 5 shows the modelled emissivity of the full SHJ cell and the cell without the front ITO. The contributions to the emissivity are broken down depending on their origin: the front stack (front ITO, p-a-Si and i-a-Si), the bulk silicon wafer, the back stack (back ITO, i-a-Si and n-a-Si), and the silver contact. Clearly visible in both cases is the absorption in the bulk silicon at energies above the bandgap which results in the solar cell photocurrent. In this same region there are also significant parasitic losses in the front stack as a result of absorption in the amorphous silicon layers.

However, at wavelengths above the bandgap the origin of the emissivity in both cells is very different. In the full SHJ structure (Fig. 5a), most of the emissivity comes from absorption in the front stack, particularly in the ITO layer. When this layer is absent, as in the second case (Fig. 5b), the emissivity is still very high but due to the absorption in the back layer stack. The high emissivity of sample 2 may seem surprising when considering the data in Fig. 5a, as the main source of absorption/emission at wavelengths longer than the bandgap of c-Si is the front stack, in which the ITO is the thickest and most highly absorbing layer. It seems likely that removing this layer would reduce the overall emissivity of the cell; however, this is not the case. While the absorption in the front stack is almost zero in the simulation of sample 2, the absorption in the back layer stack is now much higher. In both cases, the absorption in the c-Si silicon wafer is extremely low at long wavelengths. It appears that when the front stack is much less absorbing, light is still trapped very well inside the texture and most of it eventually gets absorbed in the back stack. Although the extinction coefficient of the back ITO is about an order of magnitude lower than that of the front ITO in the > 1 μm wavelength range, the back ITO layer is thicker and the absorption is non-negligible. The plots in Fig. 5 show both the total reflected power, i.e. all the light which is travelling backwards at the end of the simulation, and R_0, the light which is reflected during the first interaction of

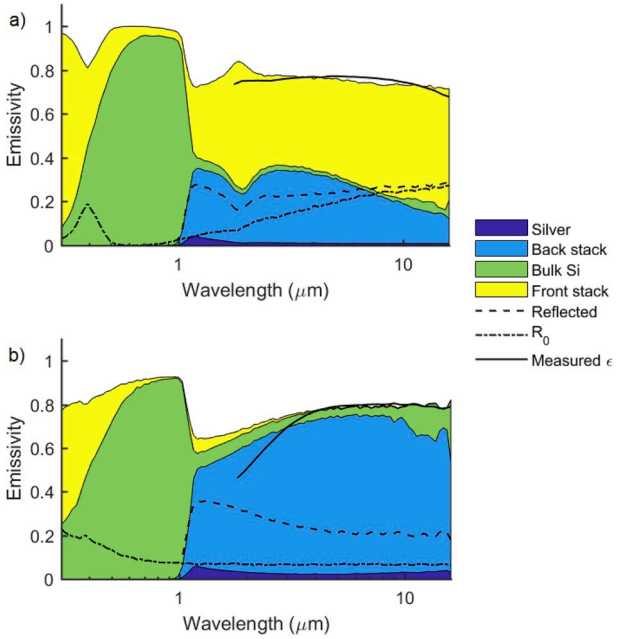

Fig. 5. Experimental and modelled emissivity results for (a) the complete SHJ cell and (b) the SHJ cell without the front ITO. The contributions to the emissivity of the different part of the cells (front, bulk, back and Ag) are shown, in addition to the total reflected power and the power reflected during the first interaction of normally incident light with the front surface (R_0).

the light with the front surface. The total reflection will be higher than R_0 if light can make at least two passes through the bulk, with some light escaping through the front surface upon subsequent interactions. Thus, at short wavelengths, where all the light is absorbed in one or two passes, $R_0 = R_{total}$, while $R_{total} > R_0$ at longer wavelengths where the bulk c-Si is more transparent. The R_0 trends for the cell with and without ITO show that while for the cell with ITO, R_0 increases towards the longest wavelengths, contributing to a reduction in emissivity (as discussed in Section 4.2), it stays very constant at < 10% for the cell without ITO for wavelengths > 1 μm. Thus, a larger fraction of the light initially enters the cell without ITO at longer wavelengths and has a chance to be absorbed.

The simulated results reproduce the measured emissivity at long wavelengths very well, as well as the trends with wavelength in both cases, supporting the above interpretation. The main discrepancies between experimental and modelled data, in the 2–4 μm wavelength range (i.e. at wavelengths above the bandgap of Si but before the onset of relatively strong free carrier absorption) are likely related to the uncertainty in the determination of the values of k when these are extremely low, where ellipsometry is not a reliable technique.

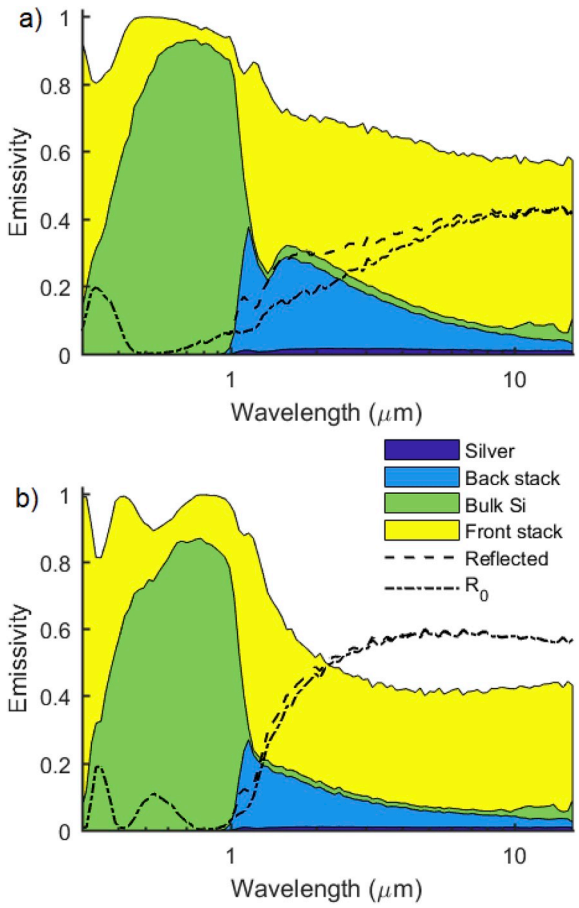

Fig. 6. Modelled emissivity results for (a) the SHJ cell with 70 nm of ITO on the front surface and (b) the SHJ cell with 160 nm of ITO on the front surface. Both cells have 70 nm of back ITO. The contributions to the emissivity of the different part of the cells (front, bulk, back and Ag) are shown, as well as the initial reflectivity (R_0) and the total power reflected.

5.2. Reducing the emissivity of SHJ cells

Fig. 6 shows the modelled emissivity of two alternative SHJ cell designs, using optical constants for ITO grown at 250 °C, which gave the lowest emissivity as measured in Ref. [3] to replace the ITO in both the front and back stacks of the SHJ cell. Fig. 6a shows a cell design with 70 nm of ITO in both the front and back stacks, while Fig. 6b shows a cell design with 160 nm of ITO in the front stack and 70 nm in the back stack. The front stack dominates the absorption in the infrared in both cases. The absorption in the front stack in Fig. 6b is somewhat reduced compared to that in Fig. 6a, even though the ITO layer in Fig. 6b is thicker; this is due to higher initial surface reflection R_0 at wavelengths above the bandgap. Less light is entering the structure in Fig. 6b, and thus the overall fraction of light which can be absorbed is reduced. However, in Fig. 6b a larger percentage of the light which enters the structure is absorbed on the first pass through the thick front ITO layer, reducing the absorption in the back stack compared to Fig. 6a.

Fig. 6a shows that the MIR emissivity in the cell design with 70 nm of ITO in the front stack is somewhat reduced from that seen in the measured SHJ cell with front ITO. However, the absorption in the bulk Si at wavelengths below the bandgap is also somewhat reduced, which would adversely affect the photocurrent. If the thickness of the front ITO is changed to 160 nm, Fig. 6b shows that the MIR emissivity can be reduced very significantly to around 40%, but the performance of the solar cell also suffers due to parasitic absorption in the front stack at energies above the Si bandgap. These results illustrate that designing an efficient cell with low emissivity at wavelengths above the Si bandgap and high absorption in the Si at wavelengths below the bandgap requires careful consideration of the material used for surface layers, their doping, and their thickness.

6. Conclusions

In this work, we have performed a thorough study of the MIR emissivity of silicon heterojunction solar cells. The absence of heavily doped silicon layers and the built-in ITO film on top, often employed as low emissivity coating, suggested this could be a silicon solar cell architecture more suitable for hybrid PV-thermal applications than the standard aluminium-diffused back contact solar cells. Our results prove that, contrary to this hypothesis, the emissivity of these solar cells is also very high, comparable to that of the standard cells, ~80% at 8 μm.

In order to track the origin of the high emissivity, the optical properties of the individual films the solar cell is made of – amorphous silicon (n-doped, p-doped and intrinsic), front and back ITO films and bulk crystalline silicon – were measured using ellipsometry, and the results used to model the emissivity of the whole cell. Our conclusion is that the ITO layers themselves are responsible for the high emissivity, taking the place of the heavily doped layers of the standard cells, and the sub-bandgap absorption in the silicon layers is negligible. Further simulations using more heavily doped ITO layers with different thicknesses show that while it is possible to reduce the emissivity of the cells, designs intended to minimize long-wavelength emissivity can also hinder the photovoltaic performance due to their parasitic absorption and increased reflectivity above the silicon bandgap.

While an optimization of the ITO layers (doping and thickness) might result in a marginal reduction of the emissivity without affecting the solar cell performance, these results, together with those published in Ref. [4] suggest that completely eliminating highly absorbing layers from the structure will be necessary. To this end, passivated emitter and rear cell (PERC) solar cells - and other variations within that family - without a continuous, highly doped rear contact, might have an advantage and should be considered in the future for hybrid PV-thermal applications [13].

Acknowledgements

This work was funded by the Engineering and Physical Sciences Research Council grant EP/M025012/1. A. Mellor was supported by the European Commission through Marie Sklodowska Curie International Fellowship, Grant No. DLV-657359. P. Pearce would like to acknowledge EPSRC CASE sponsorship from IQE plc. This material is based upon work supported in part by the National Science Foundation and the Department of Energy under NSF CA No. EEC-1041895. Any opinions, findings and conclusions or recommendations expressed in this material are those of the author(s) and do not necessarily reflect those of NSF or DOE.

Appendix A. Fitting of the ellipsometry data of the test samples

The ellipsometry data was fitted using the WVASE software from J.A. Woollam Co. combining the results obtained with a V-VASE ellipsometer for the UV-VIS-NIR range (300 nm–1700 nm) and an IR-VASE Mark-II ellipsometer for the MIR (1.7 μm–20 μm). For the ITO films, the data is fitted with a Tauc-Lorentz-Drude model as in Ref. [3]. For the silicon and amorphous silicon, the model is a general oscillator model including four separate oscillators for the above bandgap region and a Drude oscillator for the subandgap region [5]. Regions with a depolarization > 1% were excluded from the fitting. Fig. A1 shows the experimental ψ and Δ and the results of the fitting.

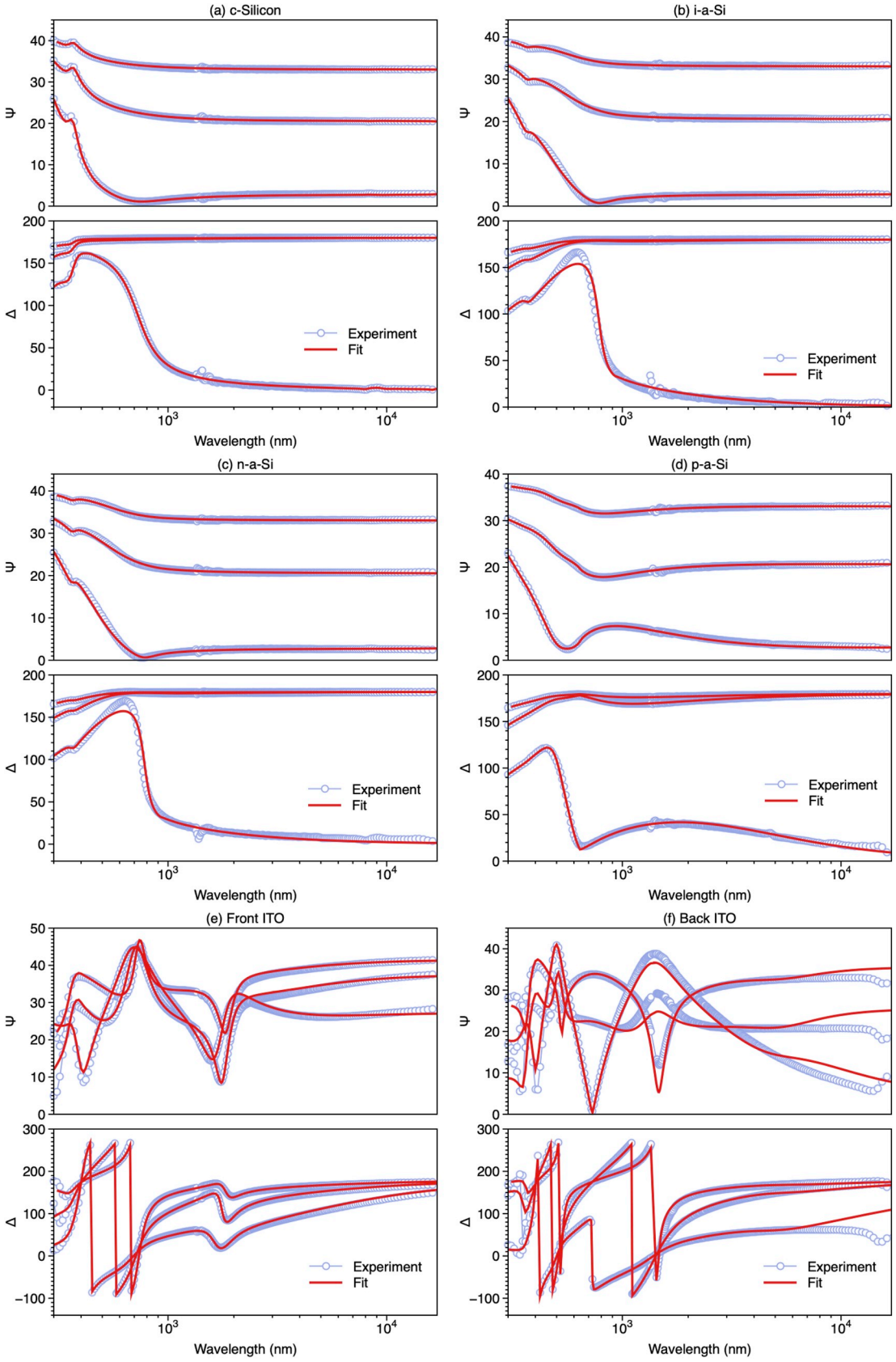

Fig. A1. Experimental and fitted ellipsometry data for the test samples including only one of the films the SHJ solar cells are made of.

References

[1] A.P. Raman, M.A. Anoma, L. Zhu, E. Rephaeli, S. Fan, Passive radiative cooling below ambient air temperature under direct sunlight, Nature 515 (7528) (Nov. 2014) 540–544.

[2] A. Mellor, D. Alonso-Álvarez, I. Guarracino, A. Ramos, A.R. Lacasta, L.F. Llin, A.J. Murrell, D.J. Paul, D. Chemisana, C.N. Markides, N.J. Ekins-Daukes, Roadmap for the next-generation of hybrid photovoltaic-thermal solar energy collectors, Sol. Energy 174 (Sep. 2018) 386–398.

[3] D. Alonso-Álvarez, L. Ferre Llin, A. Mellor, D.J. Paul, N.J. Ekins-Daukes, ITO and AZO films for low emissivity coatings in hybrid photovoltaic-thermal applications, Sol. Energy 155 (Oct. 2017) 82–92.

[4] A. Riverola, A. Mellor, D. Alonso-Álvarez, L.F. Llin, I. Guarracino, C.N. Markides, D.J. Paul, D. Chemisana, N. Ekins-Daukes, Mid-infrared emissivity of crystalline silicon solar cells, Sol. Energy Mater. Sol. Cell. 174 (Oct. 2017) 607–615.

[5] A. Augusto, S.Y. Herasimenka, R.R. King, S.G. Bowden, C. Honsberg, Analysis of the recombination mechanisms of a silicon solar cell with low bandgap-voltage offset, J. Appl. Phys. 121 (20) (May 2017) 205704.

[6] N. Tucher, J. Eisenlohr, P. Kiefel, O. Höhn, H. Hauser, M. Peters, C. Müller, J.C. Goldschmidt, B. Bläsi, 3D optical simulation formalism OPTOS for textured silicon solar cells, Optic Express 23 (24) (2015) A1720–15.

[7] N. Tucher, O. Höhn, J.C. Goldschmidt, B. Bläsi, Optical modeling of structured silicon-based tandem solar cells and module stacks, Optic Express 26 (18) (2018) A761.

[8] J.A. Woollam, Guide to Using WVASE: Spectroscopic Ellipsometry Data Acquisition and Analysis Software, (2012), pp. 1–696.

[9] E. Palik, Handbook of Optical Constants of Solids, Academic Press, Boston, 1985.

[10] C.J. Fu, Z.M. Zhang, Nanoscale radiation heat transfer for silicon at different doping levels, Int. J. Heat Mass Transf. 49 (9) (May 2006) 1703–1718.

[11] M.A. Green, Self-consistent optical parameters of intrinsic silicon at 300K including temperature coefficients, Sol. Energy Mater. Sol. Cell. 92 (11) (Nov. 2008) 1305–1310.

[12] B.L. Sopori, W. Chen, S. Abedrabbo, N.M. Ravindra, Modeling emissivity of rough and textured silicon wafers, J. Electron. Mater. 27 (12) (Dec. 1998) 1341–1346.

[13] M.A. Green, The passivated emitter and rear cell (PERC): from conception to mass production, Sol. Energy Mater. Sol. Cell. 143 (2015) 190–197.